

FAULTING OF ROCKS IN THREE-DIMENSIONAL STRAIN FIELDS I. FAILURE OF ROCKS IN POLYAXIAL, SERVO-CONTROL EXPERIMENTS

ZE'EV RECHES and JAMES H. DIETERICH

*Department of Applied Mathematics, The Weizmann Institute of Science, Rehovot (Israel) **
U.S. Geological Survey, Menlo Park, Calif. 94025 (U.S.A.)

(Received January 22, 1982; revised version accepted September 2, 1982)

ABSTRACT

Reches, Z. and Dieterich, J.H., 1983. Faulting of rocks in three-dimensional strain fields. I. Failure of rocks in polyaxial, servo-control experiments. *Tectonophysics*, 95: 111–132.

The dependence of the number of sets of faults and their orientation on the intermediate strain axis is investigated through polyaxial tests, reported here, and theoretical analysis, reported in an accompanying paper. In the experiments, cubic samples of Berea sandstone, Sierra-White and Westerly granites, and Candoro and Solnhofen limestones were loaded on their three pairs of faces by three independent, mutually perpendicular presses at room temperature. Two of the presses were servo-controlled and applied constant displacement rates throughout the experiment. Most samples display three or four sets of faults in orthorhombic symmetry. These faults form in several yielding events that follow a stage of elastic deformation. In many experiments, the maximum and the intermediate compressive stresses interchange orientations during the yielding events, where the corresponding strains are constant. The final stage of most experiments is characterized by slip along the faults.

INTRODUCTION

The orientation of small faults in samples of rocks is usually determined by axisymmetric tests in which cylindrical samples are axially loaded by a moving piston, and laterally loaded by pressure applied by a fluid or a solid (e.g. Brace, 1964; Friedman and Logan, 1973). The maximum compressive stress, σ_1 , coincides with the axial load, and the other two principal stresses, σ_2 and σ_3 , are equal to each other and to the lateral pressure. Due to this axisymmetric geometry, the dependence of fault orientation on the magnitude and sense of intermediate stress cannot be determined. We present here the results of polyaxial tests in which we determine the

* Present address: Department of Geology, Hebrew University, Jerusalem (Israel).

orientation of faults and their *pattern* under a three-dimensional strain field. During these polyaxial or "truly triaxial" tests, loads are applied on three opposite pairs of faces of cubic samples. Previous polyaxial tests deal primarily with the yielding stresses, and the orientations of faults are not presented (e.g. Hojem and Cook, 1968; Mogi, 1971; Atkinson and Ko, 1973; Paterson, 1978, p. 40).

The main incentives for the present investigation are the indications that the fault pattern in a three-dimensional strain field cannot be explained by Anderson's theory (1951) or by the theory of plasticity (Oertel, 1965). These indications include an experimental study of clay cake (Oertel, 1965), field observations of faults in sandstones (e.g. Aydin, 1977) and theoretical considerations of faulting in a three-dimensional strain field (Reches, 1978). However, the lack of experimental data for fault patterns in rocks which fail under a controlled three-dimensional strain field, limited the applications of these observations.

In this paper we present the experimental results of a series of polyaxial tests on Berea sandstone, Sierra-White granite, Candoro limestone, Solnhofen limestone and Westerly granite. We use an apparatus which maintains constant displacement rates in two axes and constant load in the third. The theoretical dependence of the fault orientations on the strain and the stress fields is derived in an accompanying paper (Reches, 1983) in which we present an analysis of faulting which assumes that faults have to accommodate the applied strain field by slip.

EXPERIMENTAL METHODS

Apparatus

Press

The deformation apparatus consists of three mutually perpendicular hydraulic presses, which independently load a cubic specimen of about $2.1 \times 2.1 \times 2.1$ cm. The apparatus is the biaxial press used by Dieterich (1978) with two modifications. The two 40-ton, hydraulic presses are servo-controlled, and a third, smaller, 5-ton, press was added. The servo system significantly increases the stiffness of the presses so that it is possible to continue deformation of a specimen after yielding without complete disintegration of the specimen.

The loading directions of the two main presses are designated by the X axis for the vertical one, and the Y axis for the horizontal one (Fig. 1). The loading direction of the third press is designated as Z . A cubic specimen is loaded through six steel anvils with polished loading surfaces of 1.9×1.9 cm (Fig. 1). Each pair of anvils, of a given axis, has a spherical surface to guarantee the alignment of the piston-specimen system.

The displacement rates of both X and Y axes are servo-controlled, using a PDP 11 as an on-line computer. Displacement rates range from 0.1 micron/sec, corresponding to strain rate of $4.8 \cdot 10^{-6} \text{ sec}^{-1}$, to about 10 microns/sec.

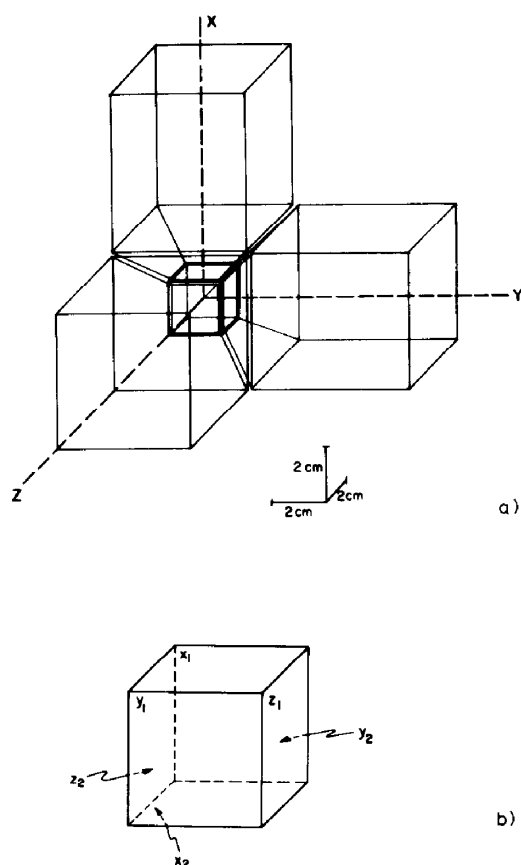


Fig. 1. a. The cubic sample and the loading anvils used in the current experiments. The sample is drawn in a heavy lines. Only three out of the six anvils are shown; each drawn anvil has an opposing anvil acting on the parallel face of the sample. The deformation axes X , Y and Z are marked. b. Location and designation of the six faces of the samples.

Instrumentation

The axial forces in the X and Y axes are determined by force gauges placed between the hydraulic pistons and the anvils. The pressure in the Z axis, which is kept constant during a single experiment, is determined by a pressure gauge with an accuracy of about 0.5 bar. The overall displacement along the three axes is measured by three Direct-Current Displacement Transducers (DCDTs), one per axis, mounted on the anvils, at a distance of about 2.0 cm from the sample. The forces and displacements in the three axes are recorded continuously with accuracies of about 1%.

Sample preparation

Samples are cut to rough cubes of about 2.25 cm each edge. All surfaces are then flattened, and a pair of faces made parallel to each other and orthogonal to the other

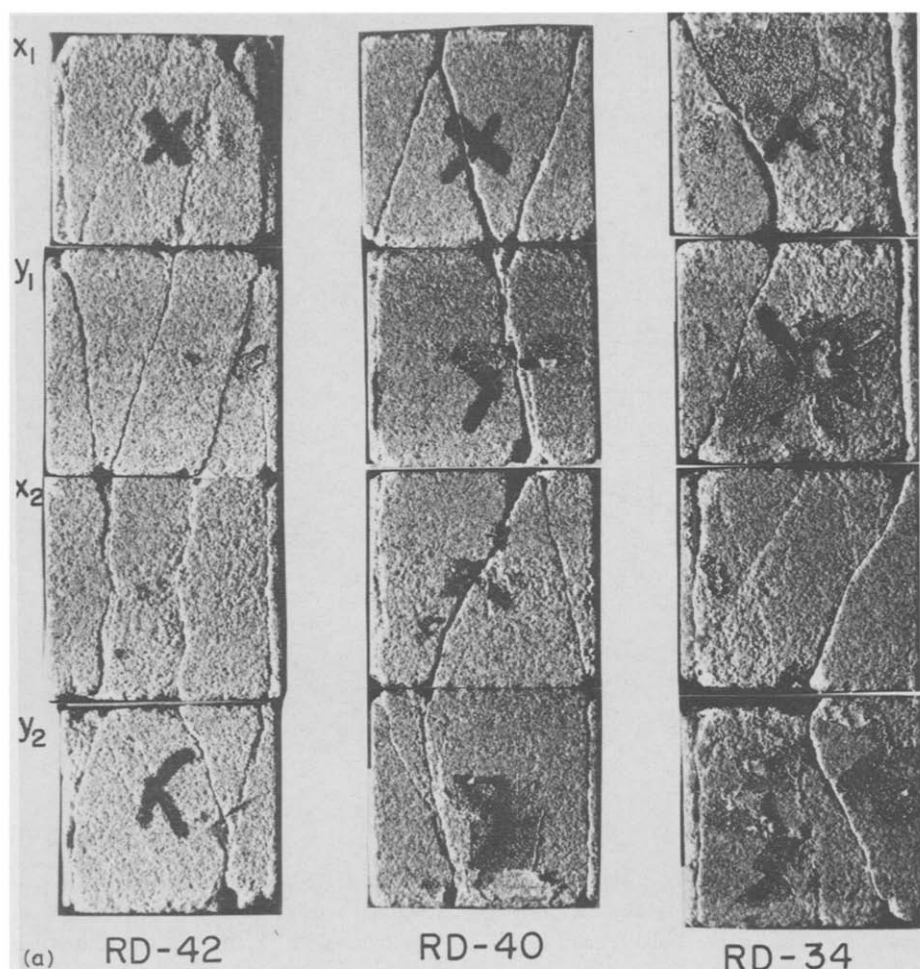
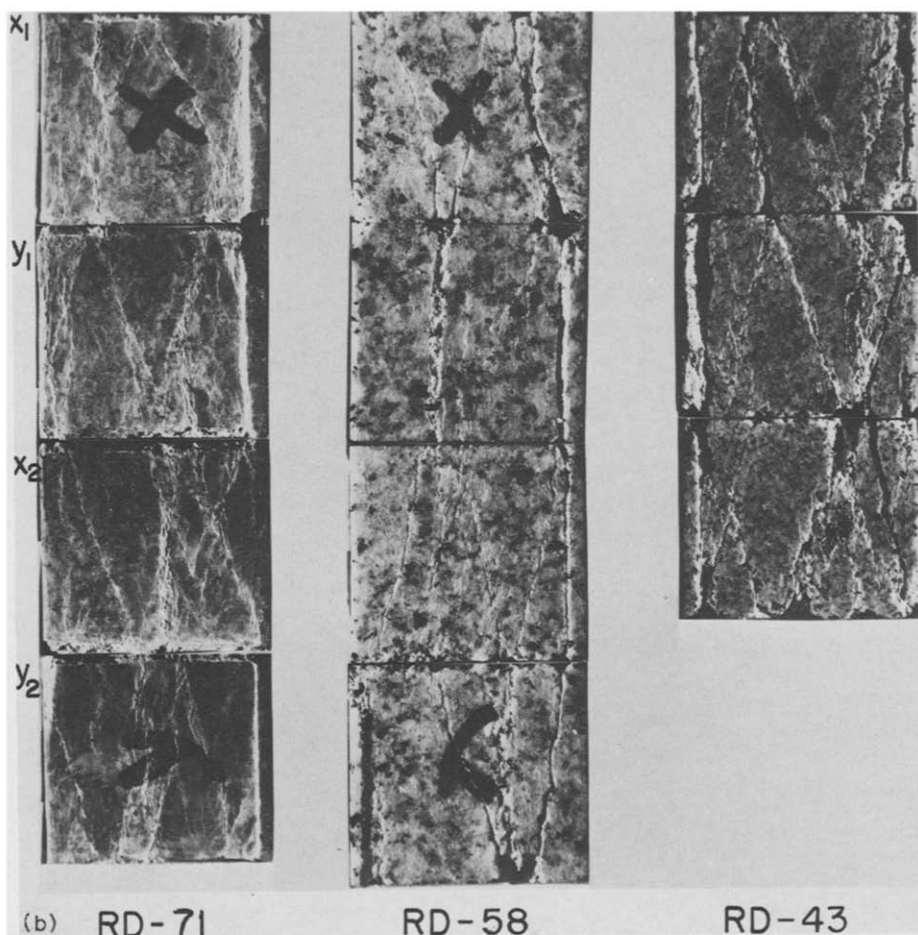


Fig. 2. The faces of deformed and faulted samples. The traces of the faults are either bright or dark lineations. In all photographs, the faces X_1 , Y_1 , X_2 and Y_2 are shown from top to bottom (see Fig. 1b). Each side of the cubes is about 2.2 cm. Dark, shining zones (e.g., faces X_1 , Y_1 and Y_2 in RD-40), are remnants of aluminium foil.

pairs by means of a surface grinder. Final dimensions of the specimens range from 2.185 cm each edge, to 2.210 cm each edge. The X , Y , and Z faces are selected and marked. In layered samples, the Z axis is set normal to the bedding. Each specimen is coated with one layer of thin aluminium foil and one layer of thin teflon.

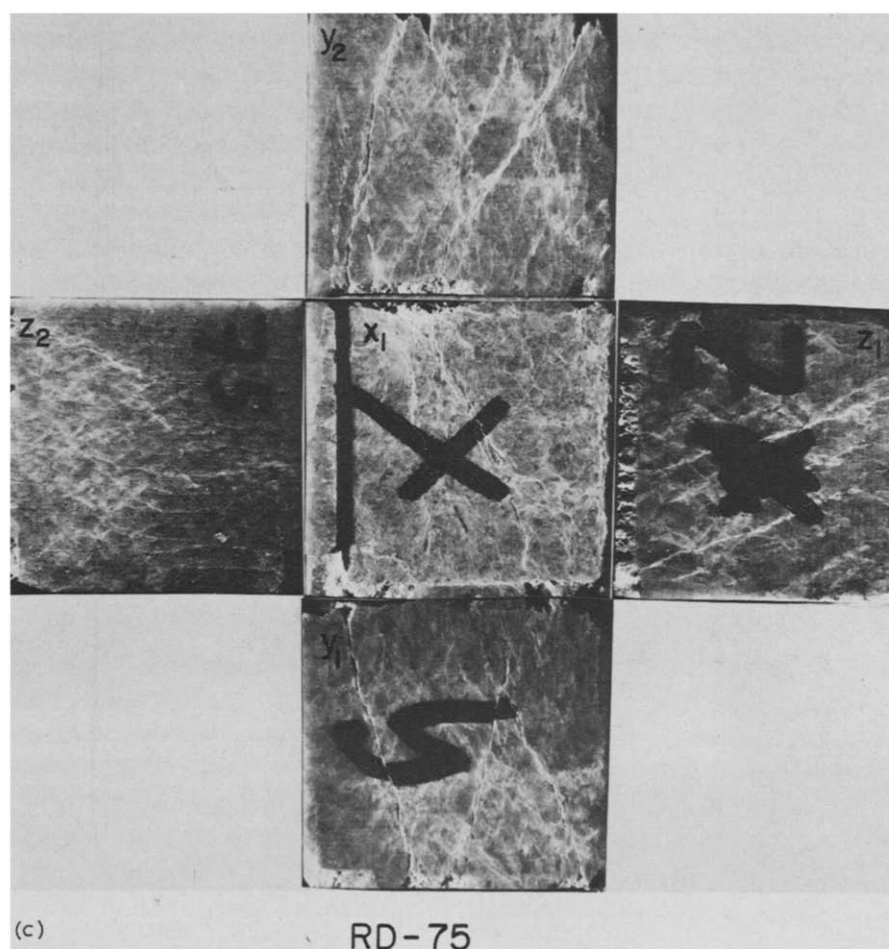
The reduction of the shear stresses on the surface of a cubic specimen is essential for the success of the polyaxial experiment (e.g. Atkinson and Ko, 1973). We reduce these stresses in the following ways: (1) Steel plates, coated with thick teflon, are inserted between each of the six anvils and the loading system. These teflon plates enable the anvils of the Y -axis, for example, to move *together* with the specimen



when displacement is applied in the X direction, and vice versa. Therefore, shear forces along the faces of the specimen are significantly reduced. (2) The thin teflon coating on the specimen reduces the coefficient of friction, and thus reduces shear stresses. Relying on these mechanisms for shear stress reduction, we consider the X , Y , and Z as the principal axes of strain and stress. The symmetry of the faults and their relatively even distribution in most experiments (Figs. 2 and 3), supports this consideration.

Rock types

We used samples of Berea sandstone, Sierra-White granite and Candoro limestone for most of the experiments. For a few additional experiments we used Westerly granite and Solnhofen limestone. These rock types, excluding the Candoro



limestone *, are commonly used in rock mechanics experiments and are described elsewhere.

Experimental procedure

In all experiments room-dried specimens at room temperature were used. The controlled displacements were always compressional in the X axis, and either compressional or extensional in the Y axis. The controlled displacements were maintained constant, therefore, the ratio of strain rates, $k = \dot{\epsilon}_y / \dot{\epsilon}_x$, were slightly modified during the tests. The largest modification of this ratio, in the present tests,

* The Candoro limestone was supplied by Candoro Marble Co. of Tennessee.

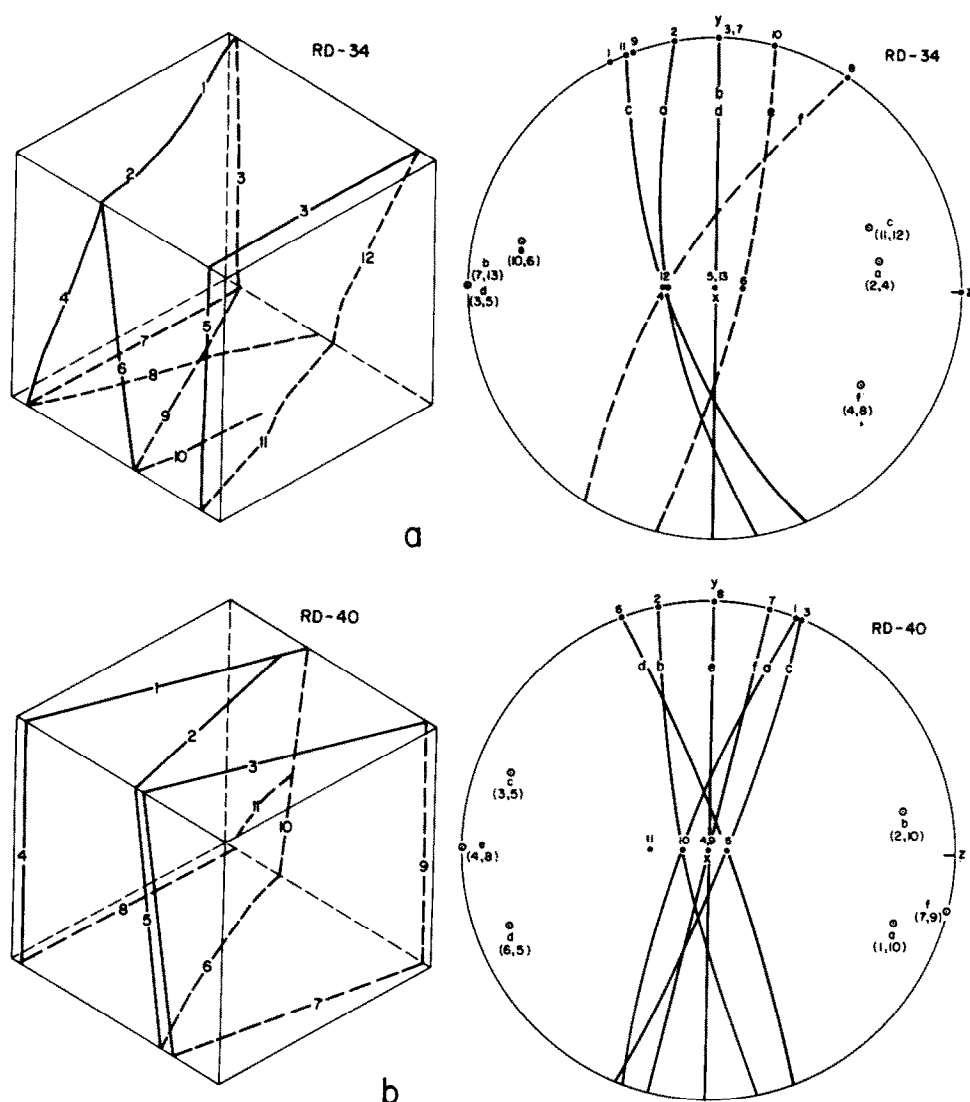
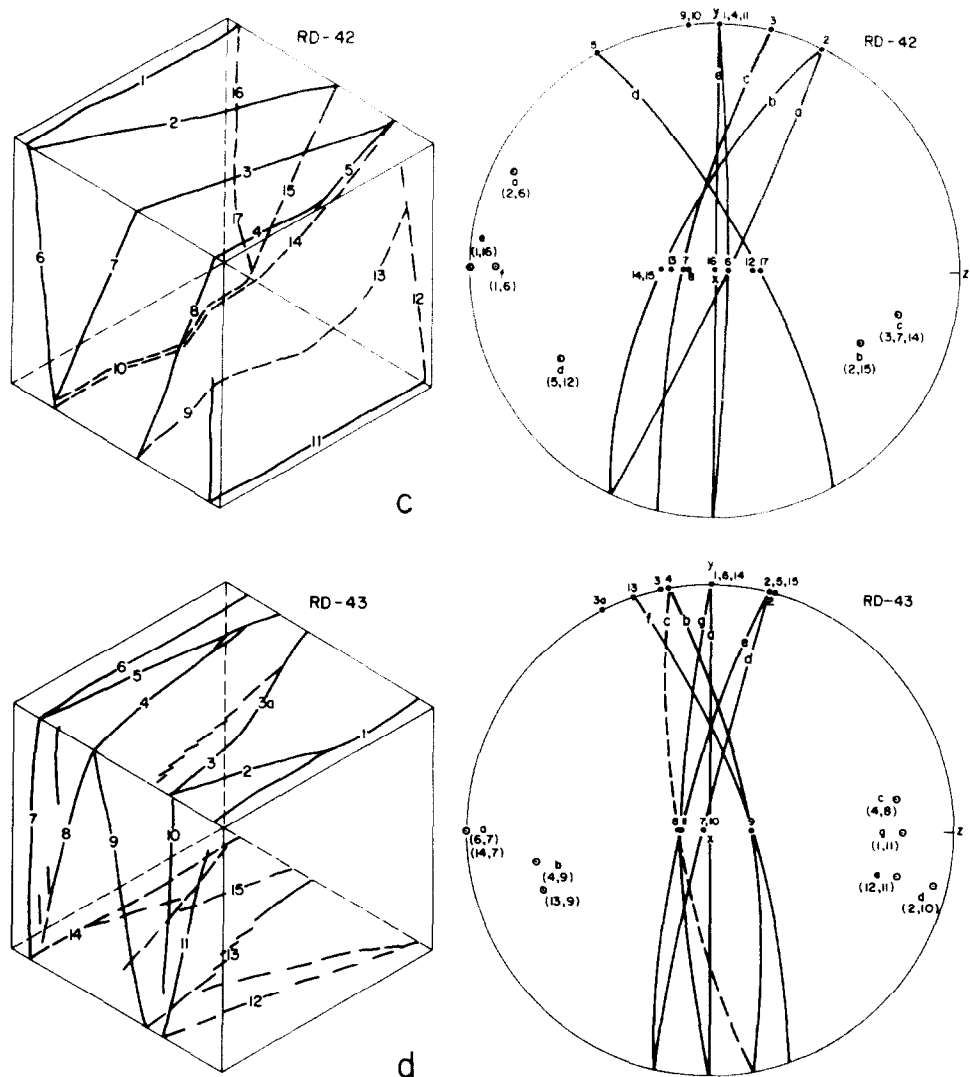


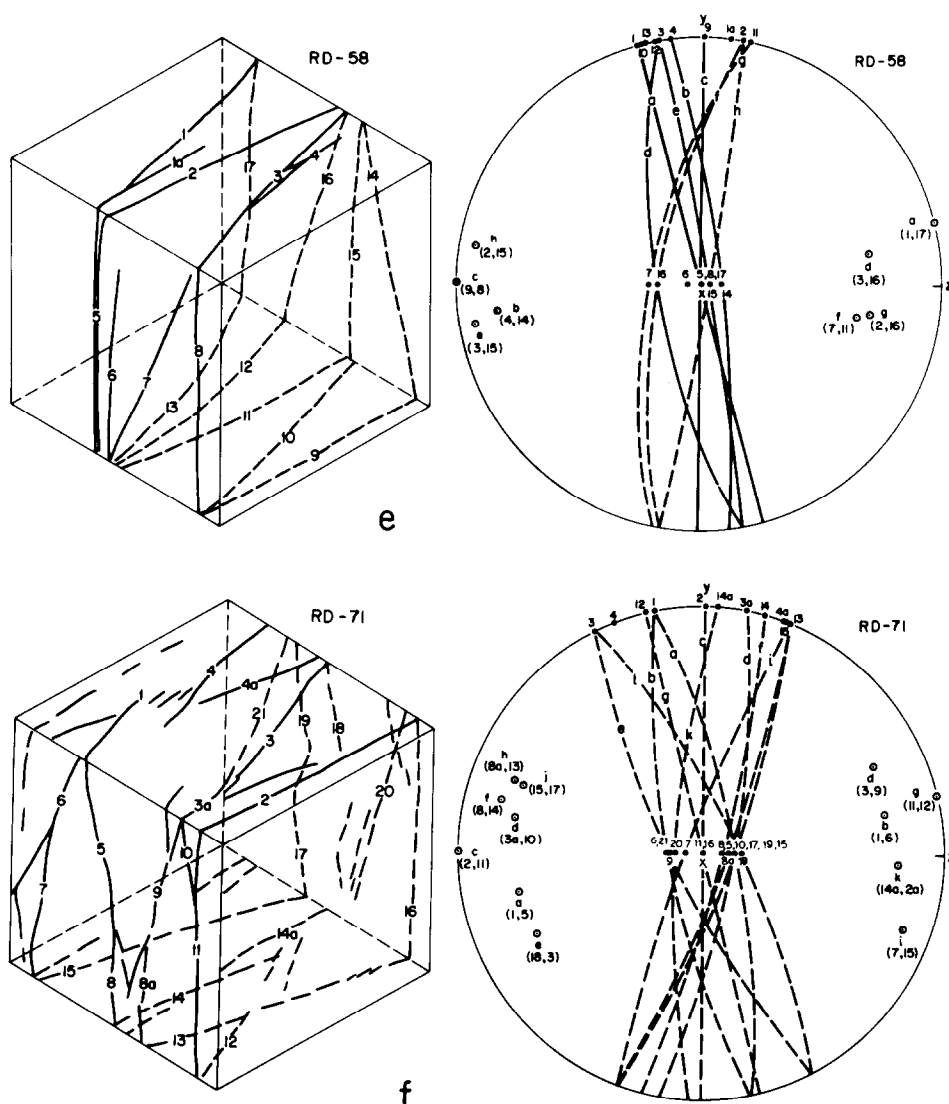
Fig. 3. The determination of the orientations of faults in six experiments. On the left side block diagrams of the faulted samples with the fault traces marked in solid line on X_1 , Y_1 and Z_1 faces and in dashed line on X_2 , Y_2 and Z_2 faces. The traces are numbered and marked on both the block diagrams and the stereonet projections (Wulff net, lower hemisphere). Traces which belong to the same fault surface are connected with a great circle, and the pole to this fault is marked and numbered. The numbers in brackets under the poles identify the traces used to recognize this fault. A dashed great circle indicates an inferred fault.

is an increase of 4.6% of the initial ratio, with mean modification of $1.7\% \pm 1.4\%$. Furthermore, one can show that the ratio of strain rates of the initial stage, $(\dot{e}_y/\dot{e}_x)_{\text{initial}}$, is also the ratio of the finite strains after any time t , $(e_y/e_x)_{\text{time}=t}$.



Below, we consider k as the ratio of initial strain rates and ratio of finite strains; we assume that the continuous slight changes of the strain rates during the tests are negligible. Strain rates ranged from $5 \cdot 10^{-6} \text{ sec}^{-1}$ to $2 \cdot 10^{-5} \text{ sec}^{-1}$. The ratio of the strain rates, $k = \dot{\epsilon}_y / \dot{\epsilon}_x$, ranges from 4.0 to -0.4 in the experiments, where $k = 0$ indicates a plane strain case. The displacement in the Z direction depended on the response of the sample.

The loads in X , Y , and Z axes are equalized before the initiation of the experiment. The loads of X and Y axes are modified by the servo-control system during the experiment whereas the load in the Z axis is maintained constant. A single run lasts for 20–60 min.



The stress-strain relationship obtained during the experiments is presented as stress-time and strain-time relations. The displacement rates in both X and Y axes are constant, so that stress-time diagrams for these axes are approximately equivalent to ordinaty stress-strain diagrams. All experiments are run to a total strain of a few percent, leading to the development of several small faults and fractures in the sample.

EXPERIMENTAL RESULTS

The main objective of this study is to determine the pattern of the faults developed in the samples. Furthermore, these experiments of brittle rocks in a stiff

TABLE I

Summary of the experimental conditions and the results of polyaxial failure tests

Experiment Number RD-series	Rock type *	$\dot{\epsilon}_x$ ($\times 10^{-5}$ sec $^{-1}$)	k ($\dot{\epsilon}_v/\dot{\epsilon}_x$)	Duration (min)	Compressive strains (%)		
					e_x	e_v	e_z
34	BS	1.15	2.0	33	2.24	4.49	-5.70
35	BS	1.15	1.5	33	2.29	3.43	-3.43
36	BS	0.45	4.0	44	1.19	4.78	-2.74
37	BS	1.15	0.0	59	4.04	0.0	-2.56
38	BS	1.15	1.5	22	1.52	2.29	-3.75
39	BS	1.15	1.0	22	1.52	1.52	-3.46
40	BS	0.45	4.0	19	0.52	2.05	-2.32
41	BS	0.9	2.0	22	1.20	2.43	-3.10
42	BS	1.8	1.0	17	1.83	1.83	-4.05
43	WG	0.45	4.0	6	0.15	0.60	-0.90
55	SWG	0.9	0.5	58	3.19	1.59	-1.81
56	SWG	1.8	0.5	37	4.12	2.04	-3.61
57	SWG	2.3	0.5	46	6.37	3.17	-3.47
58	SWG	1.8	0.75	41	4.54	3.42	-4.65
59	WG	1.8	0.75	31	3.32	2.50	-5.80
60	SWG	1.8	0.75	24	2.62	1.98	-3.39
61	SWG	1.35	1.0	32	2.59	2.59	-7.79
62	SWG	1.8	0.0	27	3.02	0.0	-4.10
64	SWG	1.8	-0.15	24	2.62	-0.40	-4.24
65	SOL	1.8	0.5	26	2.83	1.41	-5.13
66	SOL	1.8	1.0	25	2.76	2.76	-5.76
67	BS	1.8	0.75	36	3.91	2.96	-6.32
68	BS	1.8	-0.2	32	3.44	-0.69	-2.45
69	BS	1.8	1.0	22	2.43	2.39	-3.45
70	BS	1.8	0.0	24	3.07	0.0	-2.73
71	CL	1.35	1.0	28	2.31	2.29	-5.33
72	CL	1.35	0.5	26	2.15	1.06	-3.19
73	CL	1.35	0.0	26	2.13	0.0	-2.68
74	CL	1.35	-0.15	34	2.73	-0.55	-2.82
75	CL	1.8	-0.4	31	3.34	-1.35	-3.32
76	CL	1.8	-0.4	25	2.74	-1.09	-2.85

* BS—Berea sandstone, WG—Westerly granite, SWG—Sierra White granite, SOL—Solnhofen limestone, CL—Candoro limestone.

apparatus also provide valuable data about the post-yielding behavior of an already faulted sample. Accordingly, the description of the experimental results is divided

Peak stresses (kbars)			Fault pattern			Orientation of average faults (degrees)		
σ_x	σ_y	σ_z	no. of faults	no. of sets	symmetry **	θ_x	θ_y	θ_z
1.43	1.74	0.14	4	3	Or	71	72	27
1.69	1.69	0.14	5	4	Or	72	72	26
1.28	1.79	0.14	6	4	Or	85	67	24
1.35	0.30	0.08	5	2	Co	71	84	20
1.27	1.13	0.06	6	4	Or	77	72	22
1.30	1.06	0.06	4	2	Or	72	76	23
0.77	1.18	0.045	5	4	Or	82	74	18
0.82	1.31	0.045	5	3	Or	87	71	19
1.25	0.90	0.045	5	3	Or	77	72	23
2.59	3.90	0.13	6	3	Or	76	79	18
2.76	1.81	0.08		not clear				
3.48	2.31	0.10	6	3	Or	76	82	16
1.95	1.76	0.10		not clear				
3.58	2.76	0.10	7	4	Or	81	79	14
4.19	2.75	0.10	4	3	Or	79	82	14
3.10	2.89	0.10		not clear				
3.39	2.92	0.10	5	3	Or	79	84	13
3.07	0.31	0.10	6	2	Or	79	82	14
3.37	0.50	0.10	6	3	Or	72	76	23
3.14	1.90	0.10	4	3	Or	80	85	11
3.60	2.84	0.15	5	3	Or	82	82	11
1.08	0.83	0.05	5	3	Or	73	77	22
0.96	0.14	0.05	6	3	Or	72	79	22
1.35	1.31	0.10	6	3	Or	74	78	21
0.90	0.21	0.05	2	2	Co	74	89	16
2.71	1.87	0.15	11	4	Or	78	74	20
2.63	1.61	0.15	6	3	Or	72	82	20
2.15	0.71	0.15	3	2	Co	74	90	16
2.30	0.49	0.15	4	3	Or	75	82	17
2.03	0.51	0.15	6	3	Or	75	74	22
2.19	0.53	0.15	7	3	Or	76	73	22

** Or—Orthorhombic symmetry, Co—Conjugate set.

$\dot{\epsilon}_x$ = strain rate in x axes ($\times 10^5 \text{ sec}^{-1}$); k = the ratio of strain rate, $k = \dot{\epsilon}_y / \dot{\epsilon}_x$.

into two parts: the pattern of faults and the stress-strain relationship. The experimental data are summarized in Table I.

The fault patterns

The six faces of the deformed samples exhibit several faults and many small fractures (Figs. 2 and 3). Some of the samples disintegrate after the experiments into two or three blocks, by splitting along the freshly formed faults. The fault surfaces are semi-planar and curved; a few curved surfaces are composed of two coalescent semi-planar segments. For simplicity we measure the semiplanar faults and segments as planar. The traces of the faults and fractures on the faces of the deformed samples appear as distinctive bright zones of crushed original rock (Fig. 2). In many cases several faults run through the complete sample (Fig. 3), whereas in others the faults terminate within the sample. In most experiments fault traces are more clearly seen on the *X* and the *Y* faces than on the *Z* faces. Some samples show clear traces on all three faces.

The orientations of the faults, in the deformed samples were determined as follows (Fig. 3).

(a) The traces of the faults and fractures observed on the samples (Fig. 2) were mapped on block diagrams (Fig. 3, left side). The orientations of these traces with respect to the *X*, *Y* and *Z* axes were measured and plotted on stereonet (Fig. 3, right side).

(b) We identified traces on adjacent faces that are associated with the *same* fault. For example, traces 2, 5 and 6 are the intersections of a single fault with faces X_1 , Y_1 and X_2 , respectively of sample RD-40 (Fig. 3). In samples that split after the experiment, the faults were recognized directly. However, in samples that remain intact, the association between traces was deduced from their location. For example, traces 1 and 5 have a common point at the edge between faces X_1 and Y_1 of sample RD-71 (Fig. 3). We, therefore, concluded that they are associated with the same fault. It is difficult to define the fault orientation when more than two traces intersect at one point.

(c) The orientation of a fault was then determined by drawing a great circle on a stereonet through two, three or four traces, associated with this fault (Fig. 3). Repeating this process for all faults in the sample generates the complete fault pattern.

(d) Almost every sample contains one or more fractures which are about 2 mm from one of the edges of the sample, and are parallel to this edge (e.g., faults 3 and 5 in RD-34, Fig. 3). These fractures develop due to large stress concentrations at the edge of the anvils, which are narrower than the face of the sample (Fig. 1). Thus, these fractures do not reflect the global deformation of the sample, and we neglect them in the analysis.

(e) Some of the faults are composed of two segments with different orientations. For example, in experiment RD-40, fault *c* which is associated with traces 3 and 5, coalesces inside the sample with fault *f*, which is associated with traces 7 and 9 (Fig. 3).

The traces and the faults in all samples display several common features (six cases out of 28 are shown in Figs. 2 and 3). Most traces, excluding edge fractures, are not parallel to the edge of the samples on the X , Y or Z faces. Therefore, the faults associated with these traces are inclined to X , Y and Z axes; namely, the poles to most of the faults, are not located on the XY , XZ or ZY planes (Fig. 3).

Typically, there are three to eight faults in each sample. These faults can be divided into two, three or four sets. For example, we recognize three sets in sample RD-34 (Fig. 3a): set 1—faults a and c , set 2—faults b and e and set 3—fault f . Similarly, one can identify three sets in samples RD-42 and RD-43, and four sets in samples RD-40, RD-58 and RD-71. These sets are arranged in an *orthorhombic* symmetry with respect to X , Y and Z axes.

A general similarity of the orientations of the faults and their symmetry appears between experiments with three sets, and experiments with four sets (compare samples RD-34, 42, 43 with samples RD-40, 58, 71 in Fig. 3). Furthermore, the orthorhombic symmetry indicates that, in general, four sets of faults should develop. The occurrence of only three sets is analogous to the occurrence of a single fault rather than a conjugate set, in conventional triaxial experiments. Thus, we consider

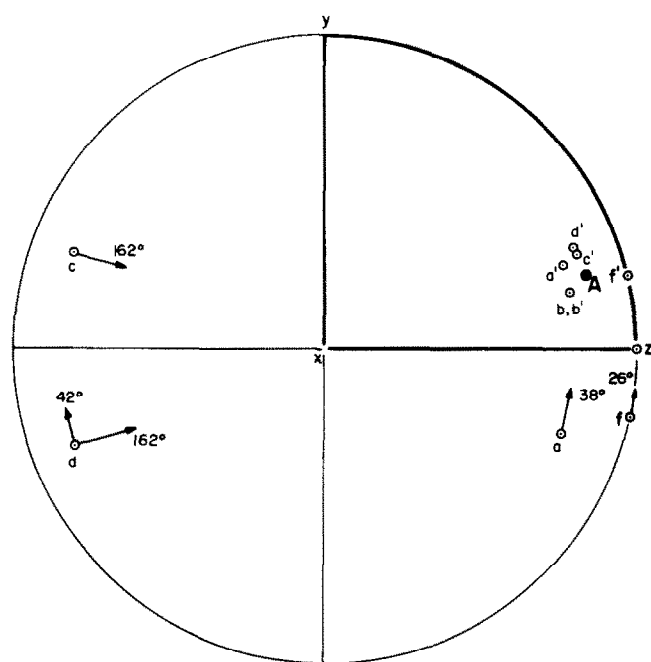


Fig. 4. The rotation of the poles to faults in experiment RD-40 according to orthorhombic symmetry into one quarter of the stereonet. Primed pole symbols indicate rotated poles, and unprimed symbols indicate unrotated. A = the average fault calculated after rotation.

fault patterns of three sets, which are distributed in three quarters of the stereonet (e.g., sample RD-34), as partially developed patterns of four sets.

When the poles to the faults are rotated according to the orthorhombic rule into one quarter of the stereonet, they cluster close to each other (Fig. 4). This clustering indicates that the four sets have similar angular relationship to the principal axes. We consider the *average fault*, (*A* in Fig. 4), calculated after rotation of all poles into one quarter of the stereonet, as the representative of all faults in the sample. When the average fault occurs on one of the principal planes, *XY*, *XZ* or *YZ*, it represents two sets in a conjugate pattern, and when this fault occurs away from the principal planes, it represents four sets of faults. The procedure described above was repeated for all samples. Table I summarizes the number of faults, the number of sets, their symmetry (orthorhombic or conjugate) and the orientation of the average fault (calculated after rotation into one quarter of the stereonet as in Fig. 4). The Fisher's standard deviation of the average faults ranges from 2.6° to 15.9° with 6.1° as mean value.

The poles to the average faults of all samples are plotted in Fig. 5 in which one can recognize the following features:

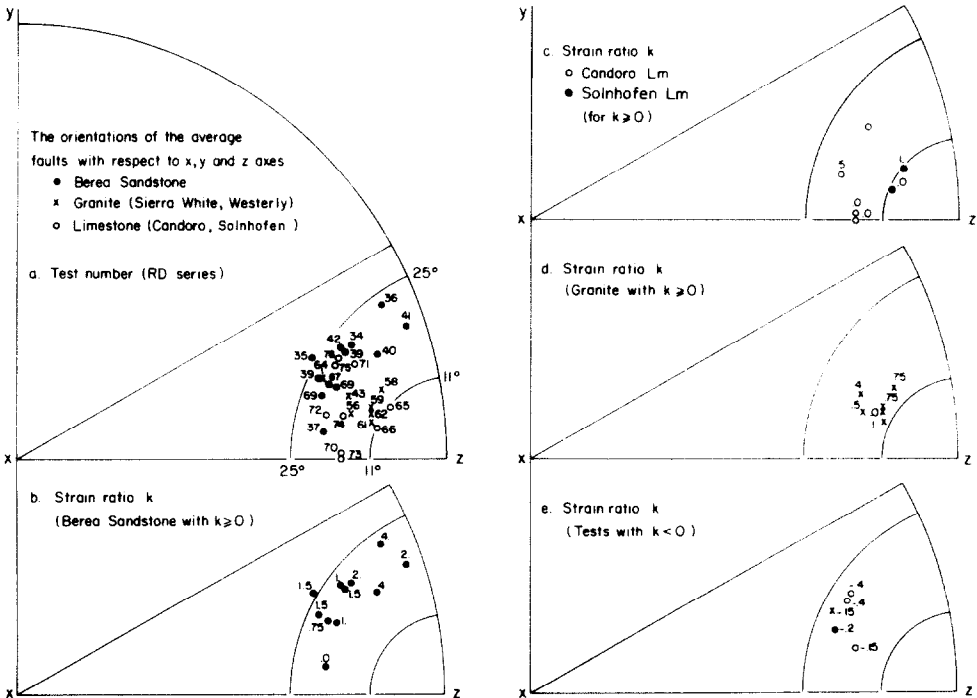


Fig. 5. The average faults of all samples plotted in a 30° section of the stereonet projection (see Fig. 4). Wulff net, lower hemisphere. The two small circles in the figure have radii of 11° and 25° around the *z* axis.

(a) The poles to all average faults are distributed between the XZ plane and the YZ plane, oriented from 11° to 25° with respect to the Z axis (Fig. 5a).

(b) The orientations of faults in the twelve samples of Berea sandstone vary systematically with the strain ratio $k = e_y/e_x$ (Fig. 5b). The faults of samples with large strain ratio, $k \geq 2$, fall close to the YZ plane, the faults of samples with intermediate strain ratio, $1.5 \geq k \geq 0.75$, fall between the XZ and the YZ planes, whereas the fault of the single sample with $k = 0$ falls closer to the XZ plane (Fig. 5b).

(c) The orientations of faults in the three samples of Candoro limestone with $k \geq 0$ (RD-71, 72, 73) and in the two samples of Solnhofen limestone (RD-65, 66), vary similarly to those of the sandstone. Faults of samples with strain ratios of $k = 1$ or $k = 0.5$ fall between the XZ and YZ planes, and the faults in the sample of $k = 0.0$ fall on the XZ plane (Fig. 5c).

(d) The poles of faults in the granite samples cluster between the XZ and YZ planes regardless of the applied strain ratio (Fig. 5d).

(e) There are only five tests, of three rock types, with negative strain ratios (Fig. 5e). The poles to the faults in these samples suggest some systematic variation where faults of $k = -0.15$ or $k = -0.2$ are closer to the XZ plane than the faults of $k = -0.4$ (Fig. 5e).

These features indicate that the fault pattern within samples of three-dimensional deformation, namely $k \neq 0$, tend to be *orthorhombic*, with *three* or *four* faults sets. On the other hand, the faults within samples which underwent plane strain, $k = 0$, tend to be arranged in a *conjugate* set with *two* fault sets. Furthermore, many samples (e.g. Figs. 5b, c) show systematic variations of the orientation of the average fault with the applied strain ratio.

Stress-strain relationship

The use of a high speed servo-controlled system in the present series of experiments makes it possible to investigate the strain-stress relationship from initial loading to post-failure behaviour of specimens under constant displacement rate conditions. The complete stress-time and strain-time relationship of three experiments are shown in Fig. 6. Partial stress-time curves of several other experiments are shown in Fig. 7. Most stress-time diagrams display three stages, marked *I*, *II* and *III* in Fig. 6. These stages may be distinguished by the following features.

Stage I is characterized by monotonously increasing stresses in both X and Y directions. For experiments with $k < 1$, σ_x is always larger than σ_y . The initial stress increase is relatively slow, followed by a constant stress increase. Similar patterns have been observed in other experiments (e.g. Paterson, 1978). The deformation during stage *I* is most probably elastic.

Stage II starts when a *yielding event* is apparent on either the σ_x or σ_y curves (Fig. 6). A yielding event is recognized by a temporary rapid stress decrease, which is

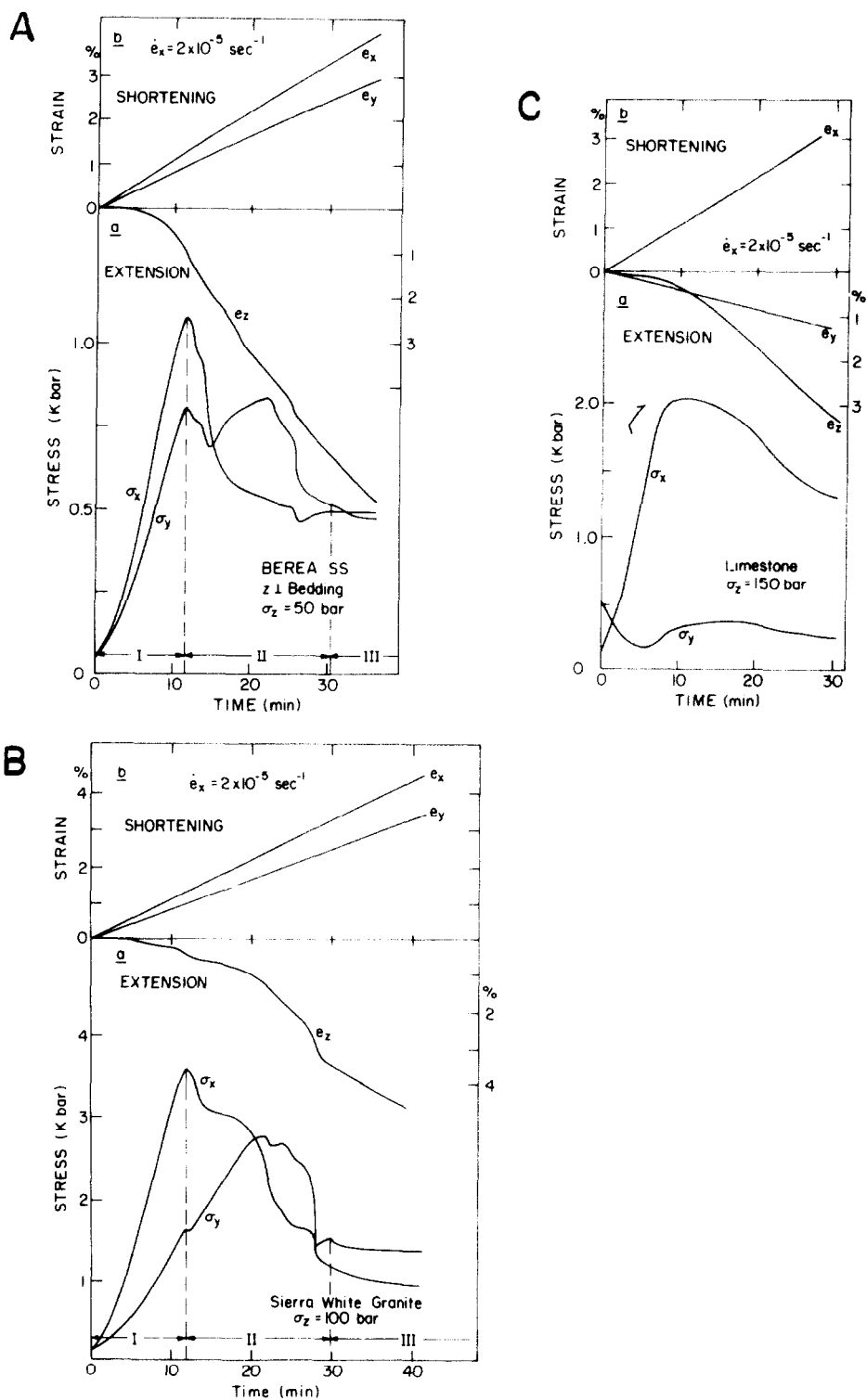


Fig. 6. The complete stress-time and strain-time curves for three experiments. A. Berea sandstone, experiment RD-67. B. Sierra-White granite, experiment RD-58. C. Candoro limestone, experiment RD-75. Note the division into three stages, I, II, and III of the stress curves in A and B.

usually preceded by a stress increase. Several characteristics of the paths of the stresses during this stage are apparent in Figs. 6A, B.

(1) The most rapid stress drop on either the X or Y axis is accompanied by a rapid stress drop on the other axis. However, there is no constant ratio between these stress drops (Figs. 6A, B).

(2) A period of a slow stress increase in the Y direction is associated with a relatively slow decrease of σ_x .

(3) The peak stress in the Y direction is always smaller than the peak stress of the X direction for $k < 1$ experiments (also see Table I). However, when σ_y reaches its peak value, during stage II, it is larger than the corresponding σ_x at that moment.

(4) The orientations of the principal stresses change during stage II. For example, the stress in the X direction, which is the maximum compressive stress, σ_1 , initially, becomes the intermediate compressive stress later (Fig. 6A, B). At the termination of stage II, either σ_x (Fig. 6A) or σ_y (Fig. 6B), may be σ_1 .

The experiments may be divided into three types according to the variation of σ_x and σ_y during stage II:

(a) Experiments with good agreement in both timing and amplitude, between the yielding events in σ_x and σ_y , and the two stress curves are similar (Fig. 7a, b, c). This type appears in experiments with strain ratios of $0.75 \leq k \leq 1.5$.

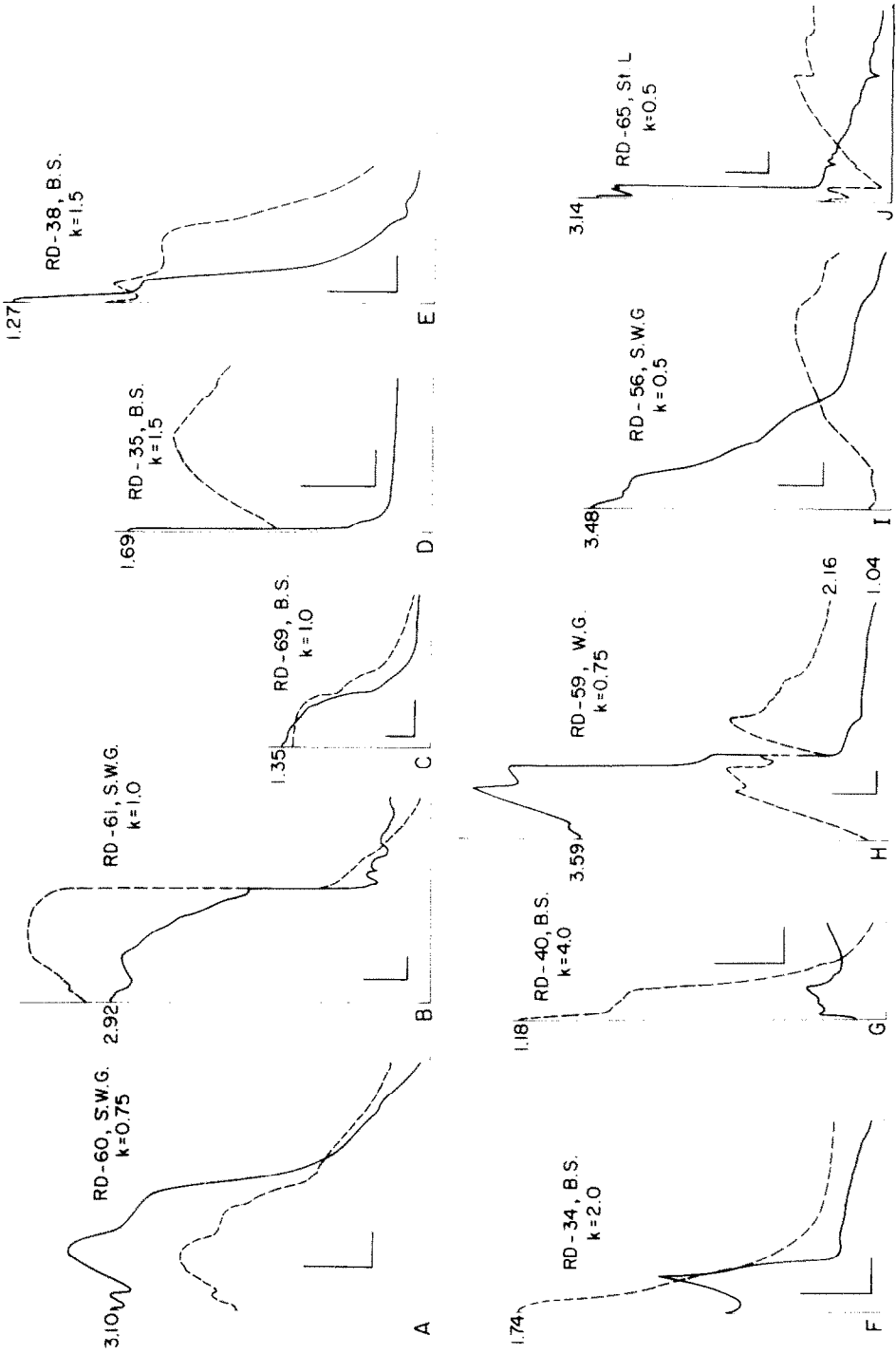
(b) Experiments with good agreement in timing between the yielding events in σ_x and σ_y . However, the amplitude of the stress drop after the yielding varies between the two axes (Fig. 7G–K). A stress increase in one axis may correspond to a stress decrease in the other. This type appears in experiments with $1.5 \leq k$ and $0.75 \geq k \geq 0.5$.

(c) Experiments with simple, continuously decreasing stresses of both σ_x and σ_y with no distinct yielding events (Figs. 7L–N). This type appears in experiments with $0.0 \geq k$.

Obviously, one may recognize transitional cases (e.g. Figs. 7D, E).

Stage III is characterized by low and relatively constant stresses in both X and Y directions. The axis of the maximum compressive stresses, σ_1 , during stage III may be either the X axis or the Y axis (Figs. 6, 7), independent of the applied strain ratio, k .

The relationships between the stress ratios, $g = \sigma_y/\sigma_x$, and the strain ratios, $k = e_y/e_x$, for all experiments, are shown in Fig. 8. Three sets of stress ratios are presented: the stress ratio during the first yielding event (initiation of stage II), the stress ratio for the second yielding event, and the stress ratio during the final stage of the experiment (stage III). The strain ratio, k , is maintained constant during the experiments. The stress ratios during the first yielding (solid dots, Fig. 8a) increase with the increase of the strain ratio. The stress ratio during the second yielding could be determined clearly only in a few experiments (crosses in Fig. 8b). It is essentially independent of the applied strain ratio. The stress ratio during the final stages of the experiments (open circles, Fig. 8b), can be divided into two groups: experiments



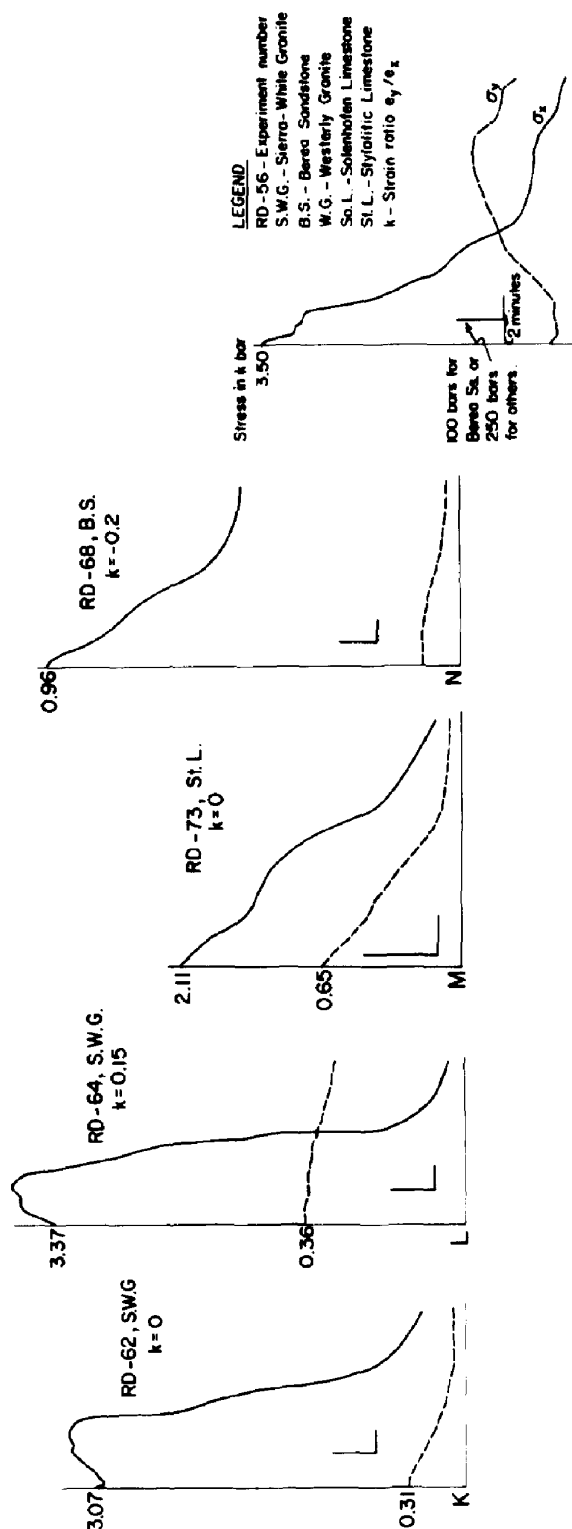


Fig. 7. The partial stress-time curves for 14 experiments. These curves were constructed by plotting the stress-time data after first yielding. The diagrams show stages II and III (Fig. 6). The values marked along the stress axis indicate the stress levels, in kbar, during first yielding. In a few diagrams (RD-62, RD-64, RD-73), the curve of either σ_x or σ_y was shifted with respect to the other. In such case the stresses of both axes are marked. Note scale bar in the legend.

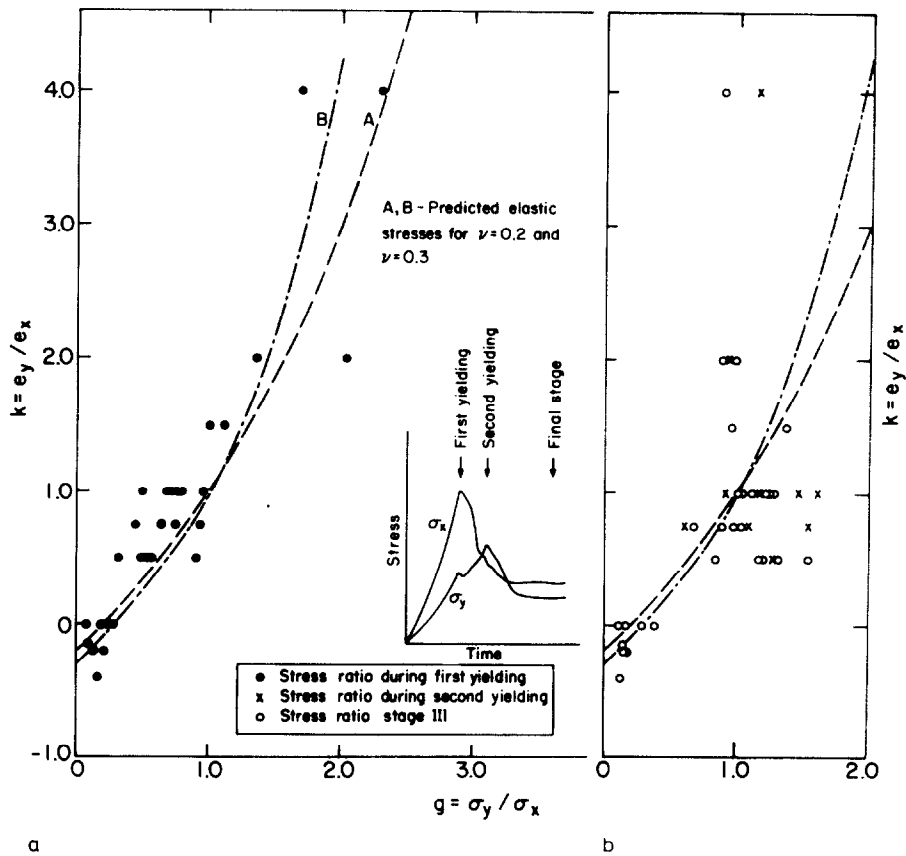


Fig. 8. The relationship between the stress-ratio $g = \sigma_y / \sigma_x$ and the strain-ratio $k = e_y / e_x$ during three moments of the experiments: the first yielding (for all experiments), second yielding (only for clear cases), final stage (only for clear cases). Curves A and B represent the theoretical distribution of the experimental stresses in homogeneous, isotropic body for $\nu = 0.2$ and $\nu = 0.3$ respectively, and $\sigma_z / \sigma_x = 0.2$ (see text).

with $k \leq 0$, in which the final stress ratio is almost the same as the ratios during first yielding, and experiments with $k > 0$, in which the final stress ratio ranges from 0.8 to 1.5, essentially independent of the applied strain ratio.

We compare these stress-strain relationships with the relationship within a homogeneous, isotropic body, before it yields or flows. These stress-strain relationships are:

$$e_x = \frac{1}{E} [\sigma_x - \nu(\sigma_y + \sigma_z)]$$

$$e_y = \frac{1}{E} [\sigma_y - \nu(\sigma_x + \sigma_z)]$$

$$e_z = \frac{1}{E} [\sigma_z - \nu(\sigma_y + \sigma_x)]$$

where E is the Young's modulus, and ν is the Poisson ratio. From the first two equations one gets:

$$\frac{\sigma_y}{\sigma_x} = \frac{k}{1 + \nu k} + \frac{\nu(1 - k)}{1 + \nu k} \frac{\sigma_z}{\sigma_x} \quad (1)$$

where $k = e_y/e_x$. Equation 1 presents the stress ratio, $g = \sigma_y/\sigma_x$, predicted for the strain ratio, $k = e_y/e_x$, in a homogeneous, isotropic body. The predicted values for $\nu = 0.2$ and $\nu = 0.3$ are plotted as curves A and B respectively in Fig. 8. The second term on the right side of eq. 1 has a negligible effect on σ_y/σ_x ; to be conservative we used $\sigma_z/\sigma_x = 0.2$, the maximum value measured in the present experiments to plot curves A and B .

The stress and strain ratios during the first yielding (solid dots in Fig. 8a) are distributed close to the predicted curves A and B . This agreement between experimental and predicted ratios, indicates that during the first yielding, and most likely during stage I as well, the samples behaved as isotropic, homogeneous bodies. However, this general agreement disappears for ratios of the second yielding and the final stage (Fig. 8b). The experimental stress-ratios range from 0.8 to 1.5 independent of the strain-ratios, for experiments with $k > 0.0$. Only experiments with $k \leq 0.0$, maintain, during the final stage, the stress-ratios of their first yielding.

The deviation of the stress-strain relationship during the second and final stage, from the stress-strain relationship predicted for isotropic, homogeneous bodies is no surprise. It is due to the highly anisotropic nature of the samples with faults and fractures that developed during the first yielding (e.g. Figs. 2 and 3). The accommodation of the applied strain by slip along these faults requires a stress field which will be derived in Part II (Reches, 1983).

SUMMARY AND CONCLUSIONS

In the present series of experiments granite, sandstone and limestone have been subjected to two- or three-dimensional strain fields. A servo-control system, which provides a stiff testing apparatus and the continuous recording of displacements and stresses makes it possible to obtain faulted yet integrated samples, as well as to study the stress history during the yielding and flow of the samples.

The orientations of the faults that developed during the experiments were determined from the traces observed on the faces of the samples (Figs. 2 and 3). In the samples one can recognize two, three or four sets of faults, arranged in a conjugate or orthorhombic symmetry with respect to the principal strain axes (Fig. 3). The fault pattern within samples which underwent three dimensional deformation, $k \neq 0$, tends to be *orthorhombic* with three or four sets; the fault pattern within samples which underwent plane strain, $k = 0$, tends to be a conjugate set with two fault sets (Fig. 5). Many samples of Berea sandstone and Candoro limestone (Fig. 5b, c) show systematic variation of the orientations of the average fault with the

strain ratio. Faults in the Sierra-White and Westerly granites have a clear orthorhombic pattern (Fig. 3). However, no systematic variation of the average faults has been observed (Fig. 5d). The variation of fault orientations will be discussed and compared in Part II to the theoretical variations.

The stresses in the two servo-controlled axes, X and Y , vary during the experiments, leading to three recognizable stages in most experiments (Fig. 6). During the first stage the stresses increase monotonously until a yielding event. During the second stage, several yielding events occur and the two principal stresses, σ_x and σ_y , vary somewhat irregularly. We recognize several types of these variations according to the timing of yielding along the two axes, X and Y , and the relative stress drops of σ_x and σ_y that follow the yielding (Fig. 7). The third stage is characterized by a slow decrease of σ_x and σ_y .

The present study indicates that, under three-dimensional strain, four sets of faults develop, rather than the two sets observed in axisymmetric, "triaxial" tests. It further indicates that the stress history during the yielding of rocks may be relatively complicated even under simple strain history.

ACKNOWLEDGEMENTS

We are indebted to Ken Harper and Gerald Conrad of the U.S. Geological Survey, whose technical assistance made this experimental work possible. We thank Andy Ruina, David Pollard, Paul Delaney and Atilla Aydin for many stimulating discussions. Arvid Johnson suggested valuable improvements to the paper. Amos Nur kindly provided most of the rock samples for this study.

The U.S. Geological Survey supported the senior author during his stay in Menlo Park, California.

REFERENCES

- Anderson, E.M., 1951. *The Dynamics of Faulting*. Oliver and Boyd, London, 183 pp.
- Atkinson, R.H. and Ko, H-Y., 1973. A fluid cushion, multiaxial cell for testing cubical rock specimens. *Int. J. Rock Mech. Min. Sci.*, 10: 351–361.
- Aydin, A., 1977. *Faulting in Sandstone*. Ph.D. Thesis, Stanford University, Stanford, Calif., 246 pp.
- Brace, W.F., 1964. Brittle fracture of rocks. In: W.R. Judd (Editor), *State of Stress in the Earth's Crust*. Elsevier, Amsterdam, pp. 110–174.
- Dieterich, J.H., 1978. Preseismic fault slip and earthquake prediction. *J. Geophys. Res.*, 83B: 3940–3948.
- Frieman, M. and Logan, J.M., 1973. Luder's band in experimentally deformed sandstone and limestone. *Geol. Soc. Am. Bull.*, 84: 1465–1476.
- Hojem, J.P.M. and Cook, N.G.W., 1969. The design and construction of a triaxial and polyaxial cell for testing rock specimens. *S. Afr. Mech. Eng.*, 18: 57–61.
- Mogi, K., 1971. Fracture and flow of rocks under high triaxial compressions. *Tectonophysics*, 76: 1255–1269.
- Oertel, G., 1965. The mechanism of faulting in clay experiments. *Tectonophysics*, 2: 343–393.
- Paterson, M.S., 1978. *Experimental Rock Deformation—The Brittle Field*. Springer. Berlin–Heidelberg, 253 pp.
- Reches, Z., 1978. Analysis of faulting in three-dimensional strain field. *Tectonophysics*, 47: 109–129.
- Reches, Z., 1983. Faulting of rocks in three-dimensional strain field. II. A strain theory of faulting. *Tectonophysics*, 95: 133–156.